Novel Electromagnetic Actuation Scheme for Multiaxis Nanopositioning

Shobhit Verma[1], Huzefa Shakir[2], and Won-Jong Kim[2]

[1]KLA-Tencor, San Jose, CA 95134 USA

[2]Mechanical Engineering Department, Texas A&M University, College Station, TX 77843-77840 USA

In this paper, we present a novel electromagnetic actuation scheme for nanoscale positioning with a six-axis magnetic-levitation (Maglev) stage, whose position resolution is 3 nm over an extended travel range of 5×5 mm in the x-y plane. We describe the conceptualization of the actuation scheme, calculation of forces, and their experimental verification in detail. This actuation scheme enables the application of forces in two perpendicular directions on a moving permanent magnet using two stationary current-carrying coils. The magnetic flux generated by the magnet is shared by the two coils, one right below and another on one side of the magnet. The magnitudes and directions of the currents in the coils govern the forces acting on the magnet, following the Lorentz-force law. We analyzed and calculated the electromagnetic forces on the moving magnet over a large travel range. We used feedback linearization to eliminate the force-gap nonlinearity in actuation. The new actuation scheme makes the Maglev stage very simple to manufacture and assemble. Also, there is no mechanical constraint on the single moving platen to remove it from the assembly. There are only three NdFeB magnets used to generate the actuation forces in all six axes. This reduces the moving-part mass significantly, which leads to less power consumption and heat generation in the entire Maglev stage. We present experimental results to demonstrate the payload and precision-positioning capabilities of the Maglev nanopositioner under abruptly and continuously varying loads. The potential applications of this Maglev nanopositioner include microfabrication and assembly, semiconductor manufacturing, nanoscale profiling, and nanoindentation.

***Index Terms*—Electromagnetic analysis, feedback linearization, multiaxis nanopositioning, permanent-magnet actuator, precision motion control.**

I. INTRODUCTION

PRECISION motion control plays a crucial role in manufacturing, manipulating, or scanning on the micro/nano level. Electromagnetic actuators have been employed as one of the best solutions for motion control applications. Various electromagnetic schemes provide wide ranges of linear or rotational motions with fine resolution. Cho *et al.* analyzed the flux density distribution of a two-dimensional (2-D) permanent-magnet array of planar motors [1]. They also designed synchronous permanent-magnet planar motors [2]. Cao *et al.* investigated three kinds of permanent-magnet arrays used in planar motors with polarity centers distributed in the lattices of a matrix [3]. The magnetic fields of these arrays were analytically compared. Guckel *et al.* developed and demonstrated a current-excited planar rotational magnetic micromotor consisting of six stator and four rotor poles [4]. This motor uses vertical reluctance force to levitate the rotor up to 50 μm. Melkote and Khorrami demonstrated closed-loop control of a 2-D linear stepper (Sawyer) motor including the rotational (yaw) degree of freedom (DOF) [5]. This motor can be applied to a high-speed accurate manufacturing system. A low-cost variable-reluctance motor for precision manufacturing automation was developed by Gan and Cheung [6].

Among many electromagnetic techniques, magnetic levitation uses electromagnetic force for levitation as well as propulsion and has been found to be very useful for precision motion control. Several research groups developed electromagnetic schemes to generate multiaxis motions using magnetic levitation. Kim *et al.* developed a fundamental framework for levitation motors and a concentrated-field magnet matrix generating constant three-dimensional (3-D) magnetic field for actuation [7], [8]. This magnet matrix was constructed by the superimposition of two orthogonal Halbach magnet arrays. The Maglev stage using this magnet matrix demonstrated a position resolution of better than 20 nm, planar travel range of 160×160 mm, and maximum velocity of 0.5 m/s at a 0.5 m/s^2 acceleration, which can enhance the throughput in precision manufacturing [9]. Jung and Baek designed and demonstrated a 6-DOF Maglev positioner with self-stability for 5 DOFs [10]. It had a position resolution of 0.5 μm in 32-mm-wide x–y planar motion and a 0.45-μm resolution in z motion. Its moving mass was 173 g. Hajjaji and Ouladsine built a nonlinear control model for long-range movement of a Maglev system and tested it by real-time control implementation [11]. A Maglev scanning stage that exibited a 0.6-nm three-sigma horizontal position noise was fabricated and demonstrated by Holmes *et al.* [12]. The development and motion control of a large-travel ultraprecision magnetic suspension stage was presented by Menq *et al.* [13], [14].

Several researchers have been working on various applications using magnetic levitation technology. Khamesee *et al.* demonstrated the use of magnetic levitation in a micro-robotic system used for transportation and assembly of miniature parts in hazardous environment [15]. This microrobot can be remotely operated in 3 DOFs in an enclosed environment by transferring magnetic energy and optical signals from outside. Hollis *et al.* developed a Maglev fine motion wrist with programmable compliance [16], [17]. The floater carries an end effector which may be used as a tool. The control unit changes the forcer coil current patterns as the fine motion device

Digital Object Identifier 10.1109/TMAG.2006.875839

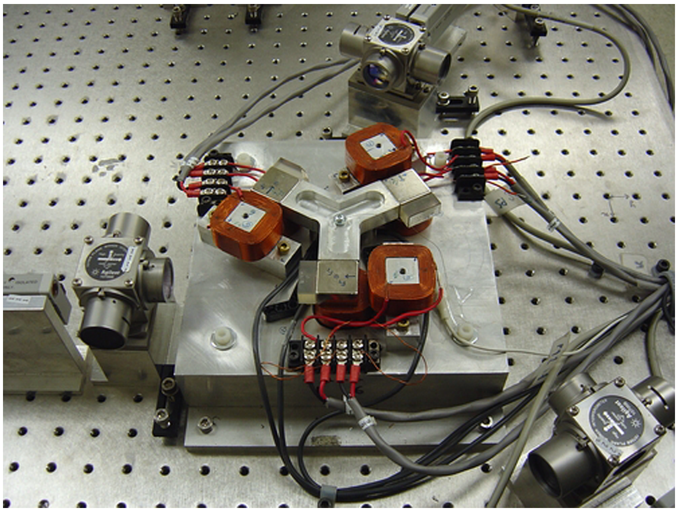

Fig. 1. Photograph of the Maglev nanopositioning stage. (Color version available online at http://ieeexplore.ieee.org.)

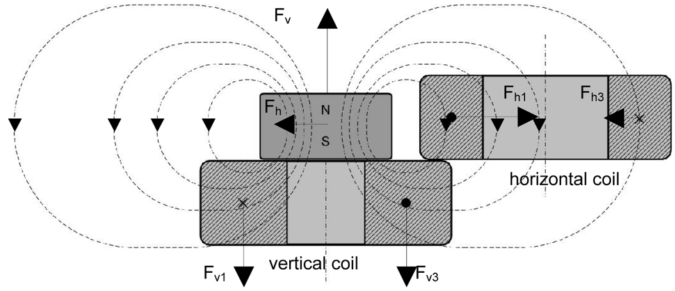

Fig. 2. Cross-sectional side view of the novel unit actuator.

approaches its final position in order to provide selected compliance in one or more DOFs. Galburt *et al.* [18], [19] developed an apparatus adapted to align a wafer in a microlithography system. It comprises a monolithic stage, a substage, an isolated reference structure, and force actuators and sensors. An optical pickup apparatus with a magnetic circuit was developed by Kano [20] which has an application in an optical-type recording and reproducing apparatus. Verma *et al.* [21] and Gu *et al.* [22] demonstrated the use of a multiaxis Maglev nanopositioner for precision manufacturing and manipulation applications, which is capable of carrying and orienting a payload up to 0.3 kg with a position resolution better than 5 nm and with a total nominal power consumption of 1 W.

The needs of high payload capacity with wide travel range at nanoscale position resolution led us to design a novel electromagnetic actuation scheme. In this paper, we present its conceptualization, design, and analysis followed by experimental verification used for the Maglev nanopositioning stage shown in Fig. 1. Its primary benefit is the reduction of the number of magnets that are the heaviest parts in the moving platen. The total mass of the Y-shaped single moving platen is 0.267 kg of which the three magnets collectively weigh 0.185 kg. This is a significant improvement compared with the Maglev stages previously developed with the moving-part masses as high as 5.58 [8] and 2.4 kg [15], maintaining the force capability high with significant mass reduction.

In magnetic levitation the moving-part mass is a very crucial design factor because a smaller mass requires less coil currents to levitate the moving part. The force required to levitate the platen against its own weight is 2.62 N. Accordingly, the average nominal current in each vertical actuator is 0.16 A. Thus, the nominal I^2R power consumption per actuator is only 144 mW to support the platen weight. Since this Maglev stage is intended to be used as a nanopositioner, even small changes in the dimensions due to thermal expansion may be significantly detrimental. The small power consumption leads to less heat generation and thermal-expansion error due to Joule losses. Hence, a consistent and repeatable positioning performance can be ensured.

Section II explains the novel actuation scheme and its benefits for multiaxis precision positioning applications. In Section III, the calculation of electromagnetic force is described. Various force equations and their parameters are given. Section IV describes the design of the vertical actuator giving continuous force to balance the levitated platen's weight against gravity. The force generated by this actuator at various positions away from the center is calculated and verified with experiments. A similar analysis for the horizontal actuator is performed in Section V. Section VI describes the need and development of the feedback linearization to eliminate the nonlinearities in the actuation, thereby improving the dynamic performance of the whole Maglev stage. In Section VII, several load tests are provided to demonstrate the Maglev stage's payload and precision-positioning capabilities under abruptly and continuously varying loads, followed by the conclusions in Section VIII.

II. Novel Electromagnetic Actuation Scheme

The novel electromagnetic force generation scheme was developed to be used in a Maglev nanopositioning stage. This scheme generates the forces in two perpendicular directions with two current-carrying coils on a single magnet. This reduces the number of magnets on the moving part and mass, heat generation, and power consumption of the stage. Fig. 2 shows a cross-sectional side view of each actuator unit. There are three such units at the three ends of the Y-shaped platen shown in Fig. 1. There are two square-shaped coils below and to the right of each magnet with the vertical magnetic axis. The terms "vertical coil" and "horizontal coil" are used for the coils to generate vertical and horizontal actuations, respectively. The coils are stationary and the magnet is attached to the moving platen. The magnetic-field lines generated by the permanent magnet are also shown in Fig. 2. The directions of the currents in flow are assumed clockwise in the vertical coil and counterclockwise in the horizontal coil, seen from the top. The directions of the forces generated in each coil section due to the assumed current flows are shown in Fig. 3.

In the vertical coil, the direction of the magnetic-field lines is normal to the direction of current flow and toward the center of the coil on all the four sides of the coil (neglecting the corner effect). Thus the $\boldsymbol{J} \times \boldsymbol{B}$ Lorentz force on the coil is vertically downwards on all the four sides of the square. The equal electromagnetic reaction force is applied vertically upwards on the moving magnet since the coil is fixed in a stationary frame.

In the horizontal coil, the direction of the magnetic-field lines is approximately downwards in all the four sides. The forces F_{h2}

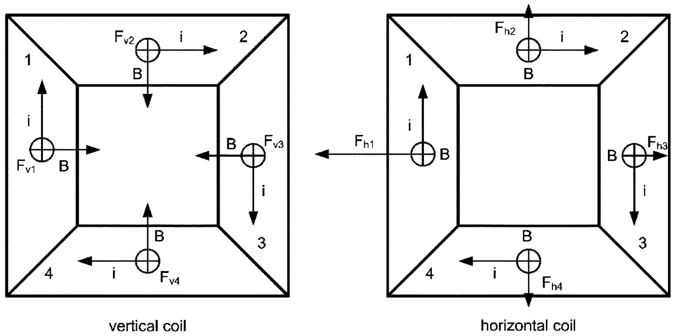

Fig. 3. Top view of the two coils in one actuation unit. The horizontal coil is displaced to the right to clearly indicate the force components.

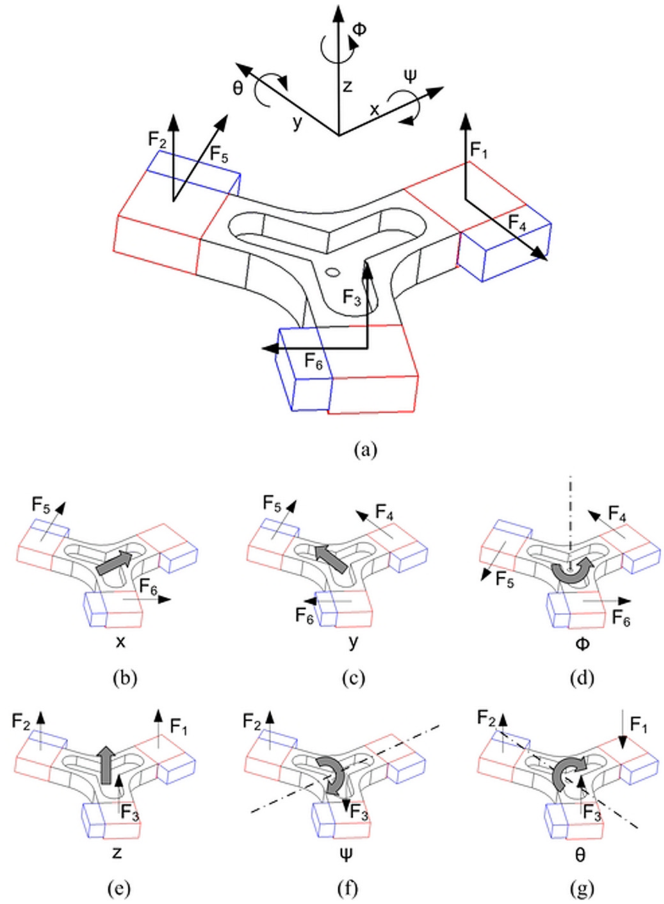

Fig. 4. (a) Convention of coordinate axes and direction of forces. (b)–(g) Conceptual modal force/torque generation in all six axes. (Color version available online at http://ieeexplore.ieee.org.)

and F_{h4} are equal in magnitude and opposite in direction due to symmetry, so they cancel. The directions of F_{h1} and F_{h3} are opposite, but the magnitude of F_{h1} is much greater than that of F_{h3} since Section 1 is much nearer to the magnet than Section 3. Thus, the effective force on the coil is to the right, and on the magnet, to the left.

To reverse the directions of the vertical and horizontal forces, we reverse the directions of current flow in the corresponding coils. To change the magnitude of the forces, we change the magnitudes of coil currents. In this manner, we can generate the forces in the two perpendicular directions independently on a single moving magnet. For six-axis motion generation, three such magnets are mounted at the ends of the Y-shaped platen, and conceptual six-axis modal force/torque generation is depicted in Fig. 4.

III. Force Calculation

The force from the interaction between the current-carrying coil and the permanent magnet is calculated by the Lorentz force law

$$\boldsymbol{f} = \int (\boldsymbol{J} \times \boldsymbol{B})\, dV \tag{1}$$

where $\boldsymbol{J}$ is the current density [A/m^2] in the coil, $\boldsymbol{B}$ is the magnetic flux density [T] generated by the permanent magnet, and dV is the small volume segment [m^3] in the coil. The limits of this integral are to cover the whole volume of the coil. After substituting the parameters shown in Fig. 5, the expression of the force acting on the volume (ς) of the coil due to the surface (Σ) magnetic charge on the magnet becomes the following quintuple integration [23]:

$$\begin{aligned}\boldsymbol{f} = &\frac{J\sigma_m}{4\pi}\iint\limits_{\mathrm{S}}\iiint\limits_{\mathrm{V}} \frac{-(x-p)\hat{k} + (z-r_2)\hat{\imath}}{[(x-p)^2+(y-q)^2+(z-r_2)^2]^{1.5}}\\ &\qquad dy\,dx\,dz\,dp\,dq\\ &-\frac{J\sigma_m}{4\pi}\iint\limits_{\mathrm{S}}\iiint\limits_{\mathrm{V}} \frac{-(x-p)\hat{k} + (z-r_1)\hat{\imath}}{[(x-p)^2+(y-q)^2+(z-r_1)^2]^{1.5}}\\ &\qquad dy\,dx\,dz\,dp\,dq\end{aligned} \tag{2}$$

where $\sigma_m = \pm\mu_0 M$ is the surface magnetic charge density on the top and bottom surfaces of the magnet with the permanent magnetization M [A/m]. The relative permeability of

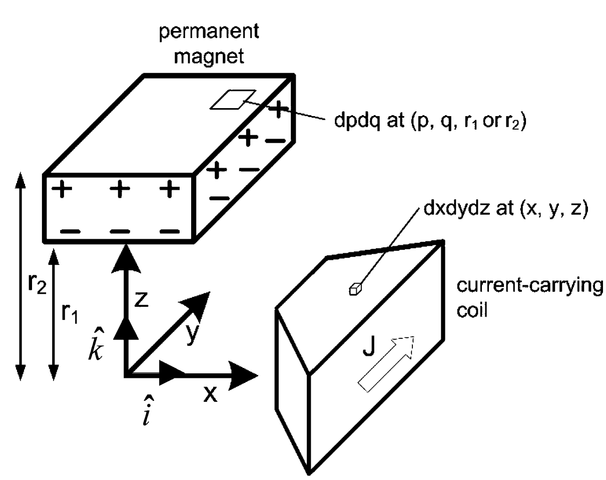

Fig. 5. Diagram indicating the parameters to calculate the force acting on magnet.

the neodymium-iron-boron (NdFeB) magnet is 1.05. Thus, we assume that its permeability is about the same as the permeability of free space μ_0 of $4\pi \times 10^{-7}$ H/m since this 5% error is within the manufacturing and assembly error of the whole Maglev stage. The unit vectors $\hat{\imath}$ and $\hat{k}$ are defined in the stationary frame attached to the coil.

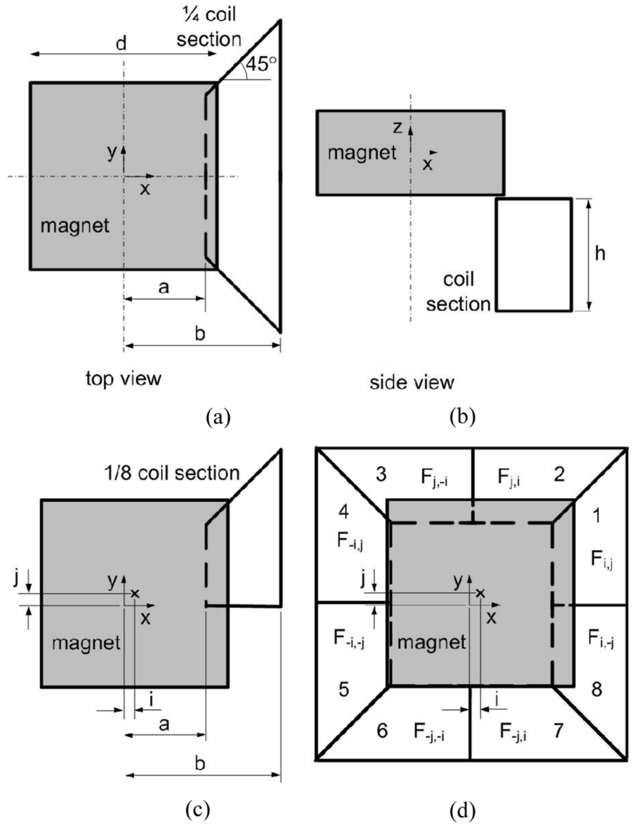

Fig. 6. (a) Top and (b) side views of the magnet and vertical-coil sections showing the definition of the parameters, and vertical force calculation at offset positions from the center using (c) a $1/8$ section of the vertical coil, and (d) the whole vertical coil indicating the partial force components.

IV. Vertical Actuation

Actuation force, platen mass, and sensor and actuator packaging are the main design issues, and several design iterations were carried out to determine the optimal sizing of the coils and the magnet. The precise calculation of the actuator's vertical force is a crucial part for the Maglev-stage design because it is the force that levitates the moving platen against gravity.

A. Actuator Sizing

To calculate the vertical force, we divide the vertical coil into four identical sections, namely Sections 1–4, as shown in Fig. 3. The horizontal force components on Sections 1 and 2 cancel those on Sections 3 and 4, respectively, because they are equal in magnitude and opposite in direction due to symmetry. The vertical components of these forces are added up, and the direction of the resultant force on the vertical coil is downwards, so on the magnet, upwards. We multiply a factor of 4 to the integral (2) with the following limits to calculate the overall vertical force:

$$\mathrm{S}:\left\{\begin{array}{c} p\in[-d/2,d/2] \\ q\in[-d/2,d/2] \end{array}\right\}$$
$$\mathrm{V}:\left\{\begin{array}{c} x\in[a,b] \\ y\in[0,x] \\ z\in[-h/2,h/2] \end{array}\right\} \tag{3}$$

where the dimensions d, h, a, and b are defined in Fig. 6(a) and (b). Their numerical values are $d = 25.4$ mm, $h = 17.5$ mm, $a = 5$ mm, and $b = 17.5$ mm, determined as follows.

The selection of the sizes of strong off-the-shelf permanent magnets with a high energy product is limited. We compared two square (25.4 × 25.4 mm) magnets with different thicknesses of 12.7 and 25.4 mm readily available in the market. For the same coil size at the same current level, the forces on the two magnets were calculated at various heights from the magnets. The forces with the bigger magnet would be only about 10% more than that with the smaller one. However, doubling the thickness of the magnet would increase the weight of the moving part by about 75%. Thus, NdFeB permanent magnets with the energy product $(\mathrm{BH}_{\max})$ of 280 kJ/m^3 (35 MGOe) and dimensions of 25.4 × 25.4 × 12.7 mm were finally chosen for the Maglev stage.

For the purpose of coil sizing for the vertical actuators, we calculated forces for different sizes of coils and compared them while considering the sensor packaging issues. On the basis of several design iterations using (3), the most convenient shape of the vertical coils turned out to be a square one to make the numerical analysis more tractable and facilitate the force calculations owing to its symmetry. A square shape is also the best to apply the maximum magnetic field on the square magnet in the available space. The outer dimension of the coil was determined so that we can pack all the coils as close and keep the size of the platen as small as possible. The coil height was decided so that the lower surface of the platen should be at the lowest sensing distance from the capacitance gauge with the platen resting on the top surface of the coil. Accordingly, the coils have an inner dimension of approximately 10 × 10 mm, outer dimension of approximately 35 × 35 mm, and thickness of 17.5 mm with 679 turns. The maximum calculated vertical force was 8.76 N by each vertical actuator at the magnet levitation height of 500 μm, which would be sufficient to levitate the 267-g platen with a significant error margin. The coils were wound with heavy-build American wire gauge (AWG) #24 copper magnet wire with an outer layer of heat-bondable epoxy coating on it.

B. Performance Analysis at Offset Positions

The force calculated above was based on the assumption that the symmetry axis of the coil passes the center of the magnet. However, the magnet is attached to the moving platen that moves horizontally up to ±2.5 mm from the center. Thus, an extensive analysis was necessary to ensure the force capability of the designed vertical actuator in the whole working planar travel range. However, evaluating the force (2) using MathCAD was a very time-consuming task. Thus, we divided the square coil in eight sections and calculated the force at offset positions due to one $1/8$ section of the coil and added up the contributions from all eight sections. Fig. 6(c) shows the offsets i in the x axis and j in the y axis. The vertical force on the magnet was calculated at every integer value of i and j in millimeters from -3 to $+3$ mm. The force due to this section of coil $F_{i,j}$ at the offset position i and j was calculated by the integral (2) with the following integration limits:

$$\mathrm{S}:\left\{\begin{array}{c} p\in[-d/2+0.001i,d/2+0.001i] \\ q\in[-d/2+0.001j,d/2+0.001j] \end{array}\right\}$$
$$\mathrm{V}:\left\{\begin{array}{c} x\in[a,b] \\ y\in[0,x] \\ z\in[-h/2,h/2] \end{array}\right\}. \tag{4}$$

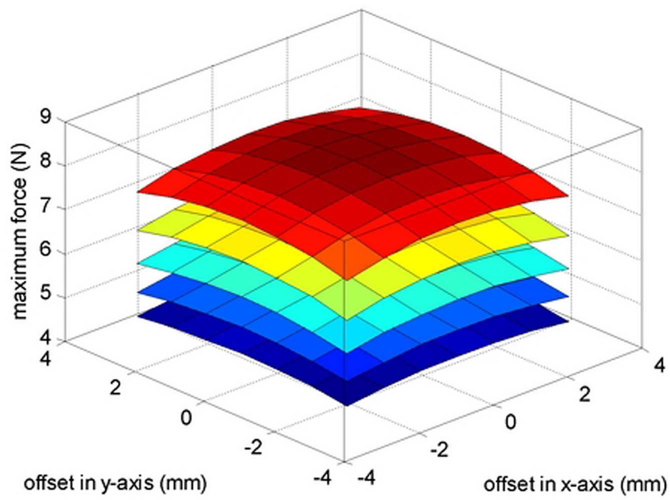

Fig. 7. Vertical forces at 49 offset positions in the x-y plane at each of the levitation heights of 1, 2, 3, 4, and 5 mm. (Color version available online at http://ieeexplore.ieee.org.)

We used this equation to find the total force generated by the whole coil. Consider the Sections 1–8 of the coil as shown in Fig. 6(d). For any offset of i and j we calculated the force component $F_{i,j}$ due to Section 1. The force due to Section 2 will be $F_{j,i}$ for the same position of the magnet. Similarly, $F_{j,-i}$ for Section 3, $F_{-i,j}$ for Section 4, $F_{-i,-j}$ for Section 5, $F_{-j,-i}$ for Section 6, $F_{-j,i}$ for Section 7, and $F_{i,-j}$ for Section 8. The summation of the forces from the individual sections gives the total force on the magnet at any offset position i and j for the whole horizontal plane of travel at a constant levitation height of the magnet.

The calculation mentioned above was performed at several different heights and using the maximum-allowable current density of 4.5×10^6 A/m^2 to prevent overheating. Fig. 7 shows the results of the calculation for the vertical force. The figure shows five surfaces for the levitation heights of 1, 2, 3, 4, and 5 mm, respectively with the topmost surface corresponding to 1 mm and bottommost, 5 mm. Each surface corresponds to the force at a fixed levitation height of the magnet and with the offset of -3 to 3 mm in the x and y axes. As the plot shows, there is a reduction in force of about 50% as the height increases from 1 to 5 mm. The actuation force also decreases notably as the magnet moves away from the center of the coil.

C. Experimental Verification

We performed experiments to verify the analytical magnetic force derived in the previous section. An experimental setup shown in Fig. 8 was designed and fabricated to measure the force between the coils and the magnet. The coils were mounted on an aluminum plate with clamps. The magnet was fixed on one end of a precision load cell. The other end of the load cell was attached to a cantilever beam that was bolted on a $xyz\phi$ positioning stage. We positioned the magnet in the three axes using screw-gauges with respect to the coils at different positions and measure the load-cell voltage output. The offset forces due to gravity and magnetic attraction were eliminated by subtracting the load-cell reading without coil current from the reading with current.

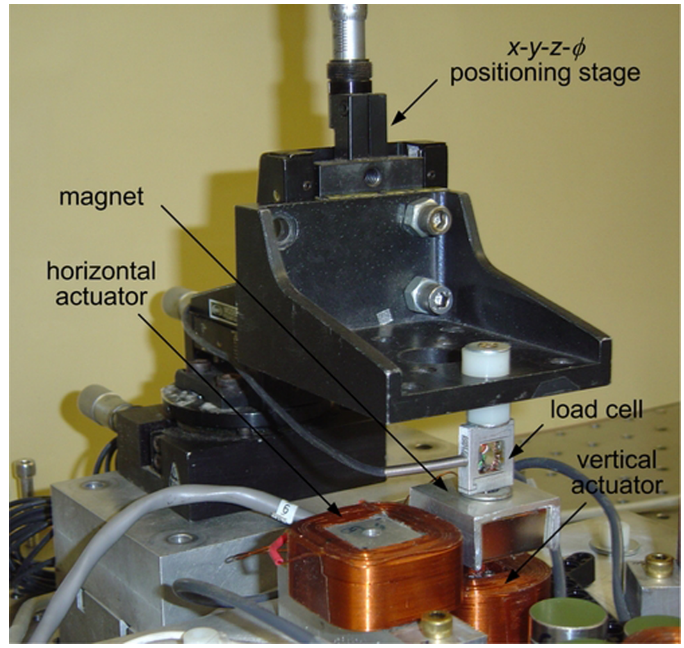

Fig. 8. Experimental setup to verify the analytical force calculation. (Color version available online at http://ieeexplore.ieee.org.)

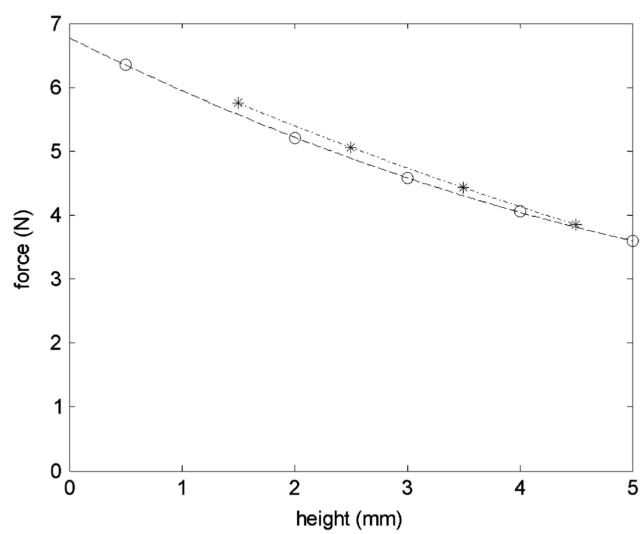

Fig. 9. Comparison of theoretical ($*$) and experimental (o) vertical forces along the symmetry axis of the coil at different heights.

Fig. 9 shows the variation of the vertical forces using a normalized current of 1 A as the magnet moved up along the symmetry axis of the coil. The actual current value used was 1.4 A, the maximum allowable current in the coil corresponding to the current density of 4.5×10^6 A/m^2. The comparison of the theoretical and experimental values proves that the estimation of the vertical force is accurate with the maximum error of only about 3%. This error is within an acceptable bound considering the errors in the reading of the fluctuating load-cell voltage due to sensor noise and mechanical errors like the backlash in the $xyz\phi$ stage.

V. Horizontal Actuation

The horizontal force contributes to the motion of the Maglev stage in the x–y plane. The force capacity of a horizontal actuator does not have to be as high as that of a vertical actuator because there is no gravity or any other external force continuously acting on the platen to be balanced horizontally. The force generated by the horizontal actuator is relatively low compared to that in the vertical direction. This is due to the larger distance between the coil and the magnet in order to have a large x-y travel range. Moreover, the farther section of the horizontal coil generates the force in the opposite direction. Hence, $F_h = F_{h1} - F_{h3}$, while $F_v = F_{v1} + F_{v2} + F_{v3} + F_{v4}$. However, we were able to size the horizontal actuator keeping the horizontal acceleration capability of greater than 20 m/s^2.

A. Actuator Sizing

Similar to the vertical coil we divide the horizontal coil in four sections as shown in Fig. 3. As shown in Fig. 2, the magnetic-field lines are approximately vertically downwards in all the sections of the horizontal coil. With the clockwise direction of the current flow assumed in Fig. 3, the directions of the forces on each section are outwards from the center of the coil. Sections 2 and 4 are located at symmetrical positions from the magnet. Thus, the forces on the two sections are equal and opposite, i.e., they cancel each other. To find the horizontal force, we calculate the forces F_{h1} and F_{h3} using the quintuple integral (2) with the integration limits (5)–(6). The parameters gap, a, b, d, and h are defined in Fig. 10. The values of gap between the magnet and the coil change with time. The dimensions a, b, and h of the coil are 10, 20, and 17.5 mm, respectively, and the width of the magnet d is 25.4 mm

$$\mathrm{S}: \left\{ \begin{array}{l} p \in [-d/2, d/2] \\ q \in [-d/2, d/2] \end{array} \right\}$$
$$\mathrm{V}: \left\{ \begin{array}{c} x \in [\mathrm{gap} + d/2, \mathrm{gap} + b - a + d/2] \\ y \in [-(-x + \mathrm{gap} + b + d/2), (-x + \mathrm{gap} + b + d/2)] \\ z \in [0, h] \end{array} \right\} \tag{5}$$

$$\mathrm{S}: \left\{ \begin{array}{l} p \in [-d/2, d/2] \\ q \in [-d/2, d/2] \end{array} \right\}$$
$$\mathrm{V}: \left\{ \begin{array}{c} x \in [\mathrm{gap} + b + a + d/2, \mathrm{gap} + 2b + d/2] \\ y \in [-(x - \mathrm{gap} - b - d/2), (x - \mathrm{gap} - b - d/2)] \\ z \in [0, h] \end{array} \right\}. \tag{6}$$

The actual horizontal force on the magnet is the difference of F_{h1} and F_{h3} (F_{h2} and F_{h4} being canceled). The coil sizing was performed by several iterations using (2) and (5)–(6). Along with providing the maximum force on the magnet, minimizing the corner effect and packaging with other parts were important issues affecting the dimensions of the horizontal coil. Like the vertical coil, the horizontal coil was determined to be a square one. The choice of a square-shaped coil and details of the size-optimization and packaging issues were discussed in Section IV-A. Since the force required from the horizontal actuators is less compared to the vertical ones, a smaller coil cross section with fewer number of turns was sufficient. Accordingly, the horizontal coil has an inner dimension of approximately 20×20 mm, outer dimension of approximately 40×40 mm, and thickness of 17.5 mm with 561 turns. Like the vertical coils the horizontal coils were wound with heavy-build AWG #24 copper magnet wire with a layer of heat-bondable epoxy coating on it. The maximum horizontal force varies from 4.5 to 2 N for the gap of from 0 to 5 mm between the coil and the magnet.

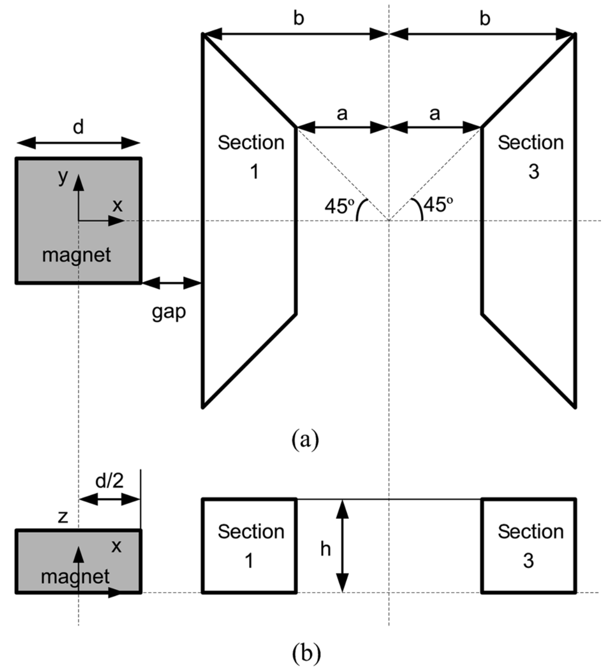

Fig. 10. (a) Top and (b) side views of the magnet and horizontal-coil arrangement.

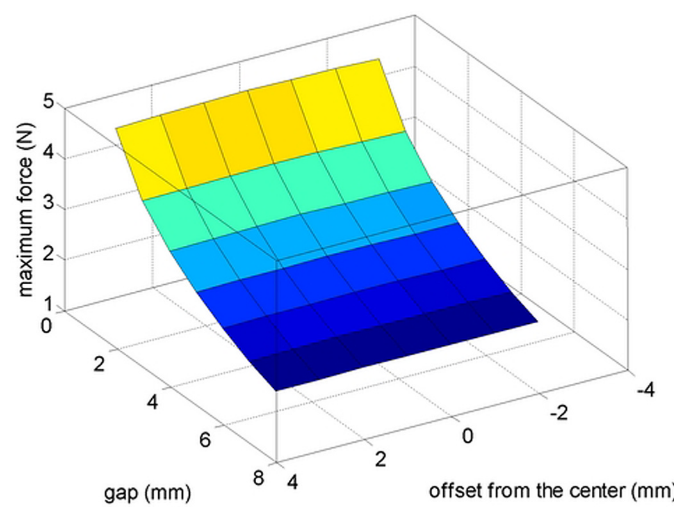

Fig. 11. Horizontal forces at offset positions. (Color version available online at http://ieeexplore.ieee.org.)

B. Performance Analysis at Offset Positions

The calculation of the horizontal force in the previous section was based on the assumption that the magnet moves only along the x axis. We estimated the force capacity of the actuator when the magnet moves in the travel range at the gap of 0 to 6.3 mm and ± 2.5 mm away from the x axis. The 3-D plot shown in Fig. 11 indicates the calculated horizontal forces at various offset positions in the whole travel volume of the stage using

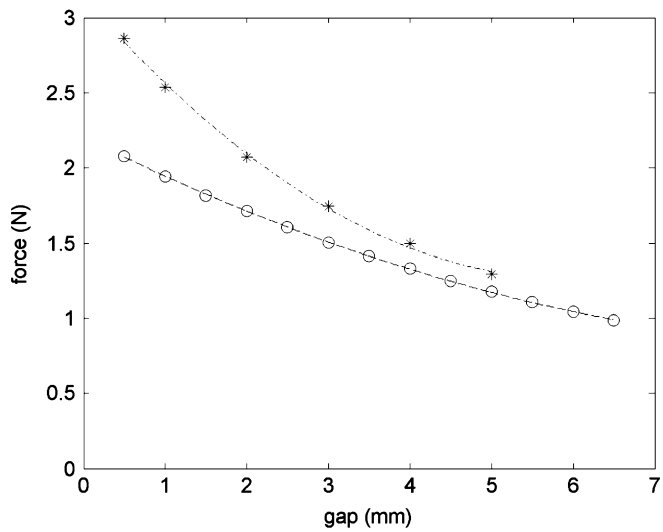

Fig. 12. Comparison of theoretical ($*$) and experimental (o) horizontal forces.

the quintuple integral (2) with the integration limits (7)–(8) and the maximum-allowable current density of 4.5×10^6 A/m^2 to prevent overheating

$$\mathcal{S}: \begin{Bmatrix} p \in [-d/2 + 0.001i, d/2 + 0.001i] \\ q \in [-d/2, d/2] \end{Bmatrix}$$
$$\mathcal{V}: \begin{Bmatrix} x \in [\mathrm{gap}+d/2, \mathrm{gap}+b-a+d/2] \\ y \in [-(-x+\mathrm{gap}+b+d/2), (-x+\mathrm{gap}+b+d/2)] \\ z \in [0, h] \end{Bmatrix} \tag{7}$$

$$\mathcal{S}: \begin{Bmatrix} p \in [-d/2 + 0.001i, d/2 + 0.001i] \\ q \in [-d/2, d/2] \end{Bmatrix}$$
$$\mathcal{V}: \begin{Bmatrix} x \in [\mathrm{gap}+b+a+d/2, \mathrm{gap}+2b+d/2] \\ y \in [-(x-\mathrm{gap}-b-d/2), (x-\mathrm{gap}-b-d/2)] \\ z \in [0, h] \end{Bmatrix}. \tag{8}$$

The motion of the magnet parallel to the closest face of the horizontal coil does not affect the force capacity much because the air gap between the magnet and the coil is small compared to their dimensions, and the fringing effect is relatively small. However, the magnitude of force drops quickly as the magnet moves away from the coil. The force reduces to almost half when the coil moves from the gap of 0.3 to 4 mm as shown in Fig. 11.

C. Experimental Verification

To verify the calculated force we performed experiments to measure the horizontal force between the coil and the magnet. Fig. 12 shows the values of the horizontal forces using a normalized current of 1 A that we achieved from the experiments and its comparison with theoretical values calculated in the previous section. The actual current value used was 1.4 A, is the maximum-allowable current in the coil corresponding to the current density of 4.5×10^6 A/m^2. This comparison shows that the maximum error between the theoretical and experimental values is up to 25% where the gap between the coil and the magnet is small. The error at the nominal gap of 3.1 mm is 12%. It is difficult to determine the gap and parallelism between the magnet and the uneven coil surface precisely, and the horizontal force drops very quickly as the gap increases, so this may be the cause for the error. Thus, for modeling purpose we decided to use the experimental values of the horizontal force.

VI. Feedback Linearization of Actuation

While modeling the actuators initially, we assumed that the force applied by the electromagnetic actuators was related to the coil current with a nominal force constant and not a function of position. However, if the translation of the permanent magnet is large, this current-to-force conversion factor is no longer constant. The forces generated by the vertical and horizontal actuators as a function of the distance between the coil and the permanent magnet are shown in Figs. 9 and 12, respectively. The forces are nonlinear functions of the gap. For a nonlinear system, controllers based on a linearized model at an operating point are only effective in a small neighborhood around that point. Out of this neighborhood, the system performance often degrades rapidly. Two approaches to the problem of ensuring consistent performance independent of the operating point have been reported in literature. One approach is the gain scheduling [24] where the nonlinear force-gap relationship of the electromagnetic actuation is successively linearized at various operating points with a suitable controller designed for each of these operating points. To ensure long travel ranges and still obtain good tracking performance, gain-scheduling controllers require the entire operating range to be broken into fine intervals and stored in large lookup tables of controller gains.

An alternative to the gain scheduling approach is feedback linearization [25]. The approach can algebraically transform a nonlinear system dynamics into a linear one, based on which linear control design methods can be applied. Feedback linearization has been proved to be a very successful technique for such systems [26]–[28]. French and Rogers used the approximate parameterization for adaptive feedback linearization [26]. Approximate state-feedback linearization using spline functions was applied by Bortoff for single-input nonlinear systems [28]. A rotating inverted pendulum was used to demonstrate the improved performance.

We used a similar approach to compensate for the nonlinearity of the Maglev system. The calculation of the desired current to generate a particular force based on (2) cannot be performed in real time because the force calculation evaluating the quintuple integrals is a very time-consuming process. Therefore, we calculated the force at several points offline and used these values to estimate the force at other points. We used the "basic fitting" function in MATLAB to find an approximate second-order polynomial function that is closest to the experimental value. Fig. 9 (dashed line with circles) shows the experimental vertical force of the actuator with a 1-A coil current, and the approximate quadratic polynomial curve is given by

$$K_v = 4.7418 \times 10^4 \mathrm{height}^2 - 8.7132 \times 10^2 \mathrm{height} + 6.7712 \tag{9}$$

where height is the height [m] of the magnet from the top surface of the coil and K_v is a nonlinear current-to-force conversion factor [N/A] in the vertical actuator. Similarly for the horizontal actuation, we calculated forces from the actuator at different horizontal gaps (gap) between the coil and the magnet

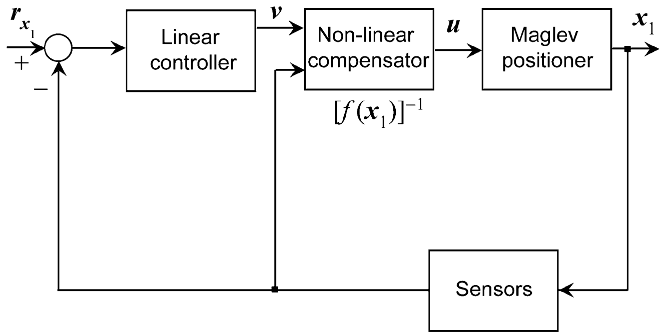

Fig. 13. Block diagram representing the feedback linearization through nonlinear compensation.

with the 1-A coil current. Fig. 12 (dashed line with circles) shows the experimental horizontal force at several gaps [m] with the 1-A coil current, and the approximate quadratic polynomial fit is given by

$$K_h = 1.3031 \times 10^4 \text{gap}^2 - 2.7161 \times 10^2 \text{gap} + 2.2050 \quad (10)$$

where K_h is a nonlinear current-to-force conversion factor [N/A] in the horizontal actuator. We can now model the plant dynamics in the following nonlinear form:

$$\begin{aligned} \dot{\boldsymbol{x}}_1 &= \boldsymbol{x}_2 \\ \dot{\boldsymbol{x}}_2 &= \frac{1}{m} f(\boldsymbol{x}_1)\boldsymbol{u} \end{aligned} \quad (11)$$

where $\boldsymbol{x}_1$ is the position vector, $\boldsymbol{x}_2$ is the velocity vector, m is the mass of the platen, and $\boldsymbol{u}$ is the coil current vector. $f(\boldsymbol{x}_1)$ consists of the modal force transformation matrix and the current-to-force conversion factors. Since the complete information on the force-gap relationship is available, we can choose the plant input $\boldsymbol{u}$ as

$$\boldsymbol{u} = [f(\boldsymbol{x}_1)]^{-1}\boldsymbol{v} \quad (12)$$

to cancel the nonlinear term. The vector $\boldsymbol{v}$ in (12) is the control efforts from the linear controllers in the form of force [N]. This cancellation results in the following linear dynamic equation of motion:

$$\begin{aligned} \dot{\boldsymbol{x}}_1 &= \boldsymbol{x}_2 \\ \dot{\boldsymbol{x}}_2 &= \frac{1}{m}\boldsymbol{v}. \end{aligned} \quad (13)$$

This feedback linearization utilizes the complete nonlinear description of the electromagnetic force and hence yields consistent performance largely independent of operating points. The block diagram shown in Fig. 13 represents the implementation of this feedback linearization approach through nonlinear compensation. The feedback linearization equations were implemented in a real-time C code to calculate the desired coil currents for a given value of force and position.

Fig. 14(a) shows the experimental result of position regulation in x. Position resolution is clearly better than 3 nm rms. Fig. 14(b), (c), and (d), respectively show the response of the Maglev stage to a reference step command of 5 mm in x and the perturbations in the other two axes, namely y and ϕ (rotation about z) with and without using feedback linearization. As

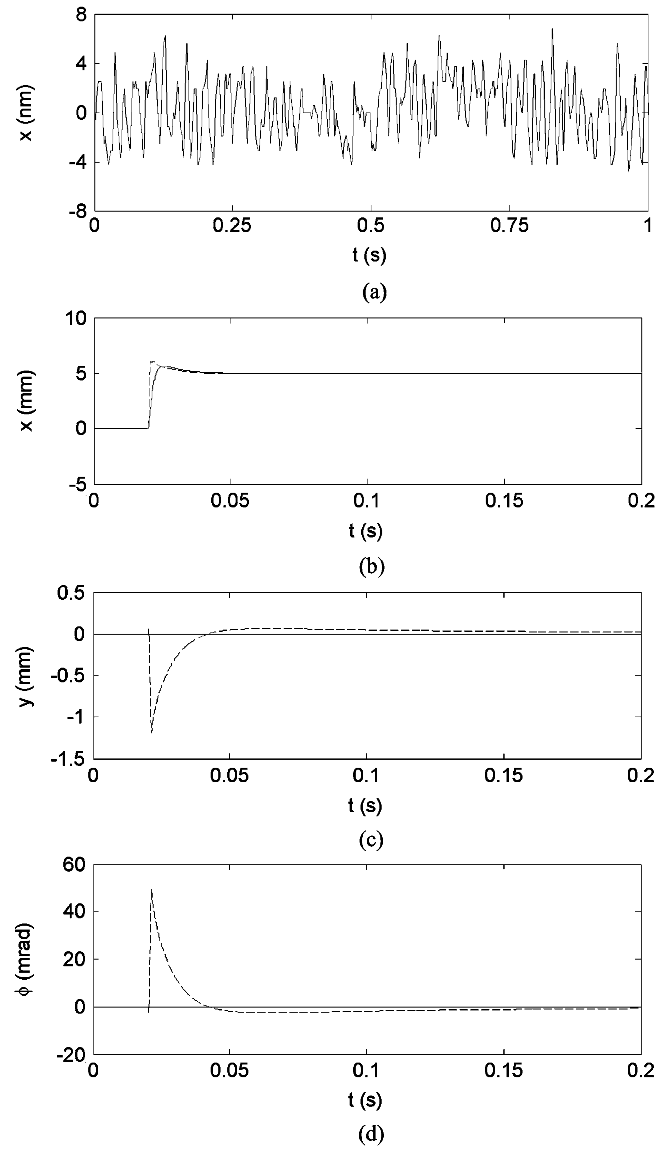

Fig. 14. (a) Position regulation in x. (b) Response of the Maglev stage to a reference step command of 5 mm in x and perturbations in (c) y and (d) ϕ with (solid line) and without (dashed–dotted line) feedback linearization.

can be seen in Fig. 14(a), the overshoot decreased from 21.3% to 12.9% with feedback linearization.

Feedback linearization also helps in reducing the effect of the stray torques acting on the levitated platen. These stray torques appear mainly due to the force imbalance when the magnet is substantially away from an operating point. If the values of i or j or both in Fig. 6(d) would be on the order of a few millimeters, the forces acting on the magnet due to the four sections of the actuator coil would be significantly different. Consequently, there will be a net moment on the magnet. Furthermore, in the absence of feedback linearization, the controller would keep applying equal current to all the three horizontal and vertical actuators. Due to the difference in the gap in individual coil-magnet pairs, however, the actual forces acting on the magnets would be different. This would result in an imbalance in the net force acting on the three magnets and there would be a net moment on the Maglev platen. Other sources of stray torques include

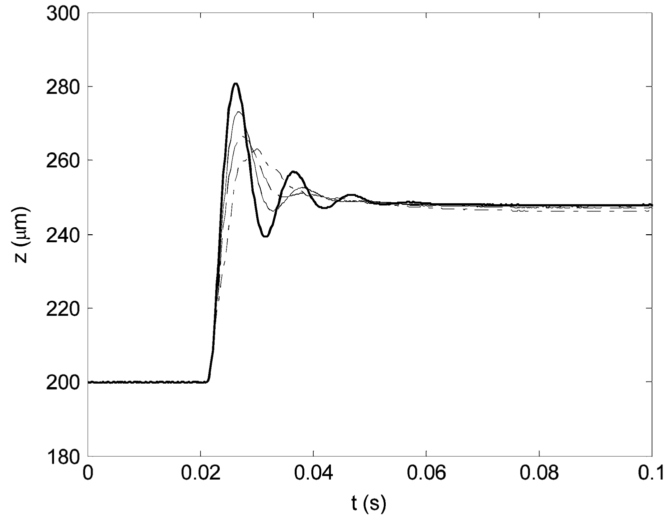

Fig. 15. No-load (thick solid line) and load tests with additional payloads of 50 g (thin solid line), 100 g (dashed line), and 200 g (dashed–dotted line).

the asymmetry in the stage structure due to mirrors and other assembly errors. Feedback linearization is again capable of effectively mitigating this problem since it uses the actual position feedback to calculate the required current. Fig. 14(b) and (c) show that there were significant deviations from the commanded regulatory positions of y and ϕ if a constant force constant was used. Feedback linearization reduced this perturbation significantly.

VII. Load Tests

It is important to analyze the dynamic behavior of the Maglev nanopositioner under load changes in order to be able to use it in practical applications like microstereolithography (μSTL), scanning, and indentation. These load changes may appear in the form of payload variations during in μSTL or as instantaneous force disturbance due to the insertion of a tool or probe tip in contact-type scanning or indentation. Accordingly, several load-tests were designed and performed on the Maglev stage to prove its precision-positioning capabilities under load changes. A proportional-integral-derivative (PID) controller with modified derivative term was designed for vertical motion control with a phase margin of 70° and crossover frequency of 65 Hz. The controller transfer function of this controller

$$C(s) = K\frac{(s+57.47)(s+6.27)}{s(s+2103)} \tag{14}$$

where K is the controller gain. The value of K for the z-axis controller is 2.32×10^5 N/m.

A. Payload Capacity

In order to test the dynamic performance of the positioner for its payload capacity, set-point-change tests were performed with different payloads. The experimental results of these tests are reported in Fig. 15. As the mass of the positioner increases with the system stiffness remaining about the same, its natural frequency decreases. Due to this reduced natural frequency, the rise and settling times increased for the increased payloads as shown in the figure. The percentage overshoot was reduced as the payload increased. With the payloads more than 200 g, the positioner went out of the range of the laser interferometer sensors for horizontal motion sensing due to excessive rotations about the x and y axes. This is because of the fact that the dead-weights could not be placed exactly at the center of the platen. Hence, a step motion in z generates stray torques about the x and y axes. However, with the sensors capable of sensing large linear and rotational motions, the current actuator design would allow additional payloads of more than 200 g.

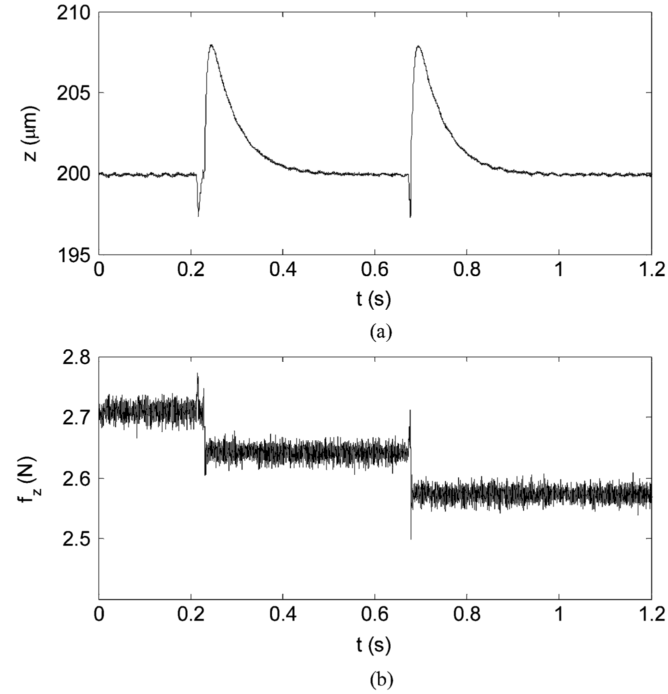

Fig. 16. (a) Position in z and (b) control effort f_z by the controller under abrupt load changes. The load changes occurred at $t = 0.21$ and 0.67 s.

B. Performance Under Abrupt Load Changes

In the applications like contact-probe-based scanning, the instantaneous disturbance due to the engagement and disengagement of the probe tip with the specimen surface may be emulated as a disturbance resulting from abrupt load changes. In nanoindentation, a stiff atomic force microscope (AFM) tip may be fixed to the base to make indents or scratches and write small letters or draw tiny shapes on a silicon substrate mounted on the moving platen. In such an application, the process of making indents with the cantilever tip may be treated as load disturbance. Although the disturbance is not expected to exceed more than a few milli-newtons in these applications, our Maglev positioner demonstrates precision positioning under the abrupt load variations on the order of 100 mN.

Fig. 16 shows the performance of the Maglev stage with abrupt load changes. Small 7.5-g plastic cylinders were used as additional loads. Fig. 16(a) and (b) respectively show the plots of the z-axis position and the control effort by the controller to recover the position of the platen when the two cylinders were taken off one at a time. The vertical actuators supplied the forces to precisely balance the weight of the platen and the payload

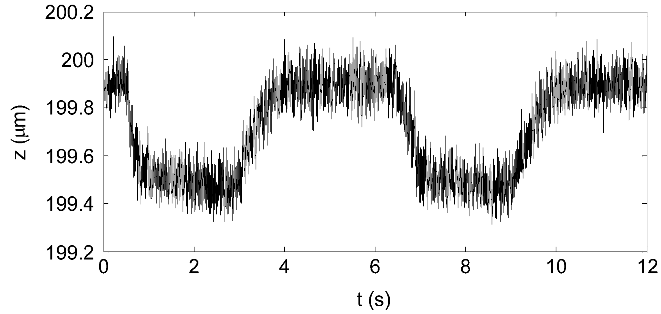

(a)

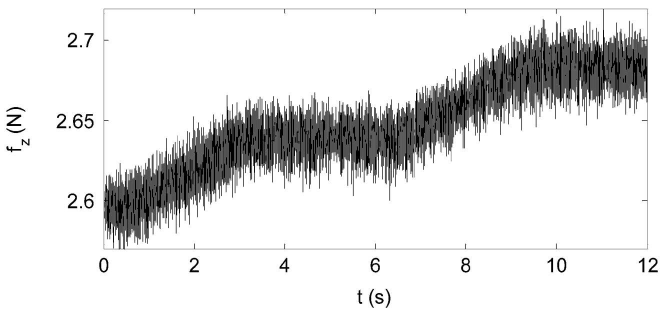

(b)

Fig. 17. (a) Position in z and (b) control effort f_z by the controller under continuously varying load.

in the beginning of this experiment. As soon as the payload was removed, the applied force instantaneously became greater than that is required to balance the weight of the platen and the payload. This excessive force gave the platen an instantaneous upward push, which was recovered by the controller over a period of 0.2 s. The Maglev system's dynamic behavior was found to be repeatable for the second load removal. It can be observed from Fig. 16(b) that the drop in the control effort as each cylinder was removed was approximately 70 mN. This matches with the actual weight of the plastic cylinders with an error of merely 5%.

C. Performance Under Continuously Varying Loads

External forces may also appear in the form of continuous payload variation or mass fluctuation. For instance, in μSTL, the mass of the substrate varies as the photopolymer is solidified. In this subsection, we demonstrate the effectiveness of the Maglev positioner to recover from such load variations. Apparently, the anticipated load variation in any of the practical applications working at micro- or nanoscale is much less than the demonstrated load capacity of the Maglev stage under continuously varying loads.

To emulate the effect of the continuously varying mass in nanomanufacturing applications, we used a continuous flow of salt falling into a bowl placed on the platen. Fig. 17(a) and (b) respectively show the position of the platen in the z axis and the corresponding control effort by the controller. The platen is levitated at a height of 200 μm. From this initial steady-state position, the mass inflow was initiated at 0.5 s and was stopped at 4 s; then started again at 6.5 s and stopped at 10 s. The total mass of the salt dropped was 5 g each time. Since the rate of the mass flow was almost constant at 1.43 g/s, the control effort linearly increased to balance the additional mass on the platen and to recover the vertical position of the platen to the steady state. However, there was a small steady-state error in the vertical position during the mass in-flow, which may be considered as a constant force disturbance. This is due to the fact that the controller (14) was designed with a single pole at the origin, to meet the zero-steady-state error requirement for the position inputs only. Accordingly, for ramp or acceleration/force inputs, the tracking error is not zero. However, immediately after the force disturbance was removed, the steady-state error became zero, which demonstrates the controller's effectiveness and the fast closed-loop dynamics.

VIII. Conclusion

Multiaxis nanopositioning stages are necessary for the manufacture and assembly of micro/nanoscale devices. Efficient and well-controlled actuation is essential for such stages. In this paper, we described the conceptualization and design of a novel electromagnetic actuation scheme capable of the force generation in two perpendicular directions using just one magnet.

An extensive analysis of the actuator performance over the whole travel range was performed and compared with the experimental forces. This comparison showed that the calculations provide a fairly accurate estimation of the forces generated by the horizontal and vertical actuators. Feedback linearization control was developed to eliminate the effect of the nonlinear force-gap relationship of the actuators.

A six-axis Maglev nanopositioning stage was developed and fabricated using the actuation scheme described in this paper. The stage achieved a 3 nm position resolution over an extended travel range of 5×5 mm in the x–y plane. Several experimental results on load tests were presented, and the precision positioning capabilities of the Maglev nanopositioner under abruptly and continuously varying loads were successfully demonstrated.

Acknowledgment

This material is based on the work supported by the National Science Foundation under Grant CMS-0116642.

References

[1] H.-S. Cho, C.-H. Im, and H.-K. Jung, "Magnetic field analysis of 2-D permanent magnet array for planar motor," *IEEE Trans. Magn.*, vol. 37, no. 5, pp. 3762–3766, Sep. 2001.
[2] H.-S. Cho and H.-K. Jung, "Analysis and design of synchronous permanent-magnet planar motors," *IEEE Trans. Energy Convers.*, vol. 17, no. 4, pp. 492–499, Dec. 2002.
[3] J. Cao, Y. Jhu, J. Wang, W. Yin, and G. Duan, "Analysis and comparison of two-dimensional permanent-magnet arrays for planar motor," *IEEE Trans. Magn.*, vol. 40, no. 6, pp. 3490–3494, Nov. 2004.
[4] H. Guckel, T. R. Christenson, K. J. Skrobis, T. S. Jung, J. Klein, K. V. Hartojo, and I. Widjaja, "A first functional current excited planar rotational magnetic micromotor," in *IEEE Proc. MEMS*, Feb. 1993, pp. 7–11.
[5] H. Melkote and F. Khorrami, "Closed-loop control of a base XY stage with rotational degree-of-freedom for a high-speed ultra-accurate manufacturing system," in *Proc. 1999 IEEE Int. Conf. Robotics and Automation*, Detroit, MI, May 1999, pp. 1812–1817.
[6] W.-C. Gan and N. C. Cheung, "Development and control of a low-cost linear variable-reluctance motor for precision manufacturing automation," *IEEE/ASME Trans. Mechatronics*, vol. 8, no. 3, pp. 326–333, Sep. 2003.

[7] D. L. Trumper, W.-J. Kim, and M. E. Williams, "Design and analysis framework for permanent-magnet machines," *IEEE Trans. Ind. Appl.*, vol. 32, no. 2, pp. 371–379, Mar. 1996.
[8] W.-J. Kim, "High-precision planar magnetic levitation," Ph.D. dissertation, Massachusetts Institute of Technology, Cambridge, MA, Jun. 1997.
[9] W.-J. Kim, N. D. Bhat, and T. Hu, "Integrated multidimensional positioner for precision manufacturing," *J. Eng. Manufact.*, vol. 218, no. 4, pp. 431–442, Apr. 2004.
[10] K. S. Jung and Y. S. Baek, "Study on a novel contact-free planar system using direct drive DC coils and permanent magnets," *IEEE/ASME Trans. Mechatronics*, vol. 7, no. 2, pp. 35–43, Mar. 2002.
[11] A. E. Hajjaji and M. Ouladsine, "Modeling and nonlinear control of magnetic levitation systems," *IEEE Trans. Ind. Electron.*, vol. 48, no. 4, pp. 831–838, Aug. 2001.
[12] M. Holmes, R. Hocken, and D. L. Trumper, "The long-range scanning stage: A novel platform for scanned-probe microscopy," *Precision Eng.*, vol. 24, no. 3, pp. 191–209, Jul. 2000.
[13] S. K. Kuo, X. Shan, and C. H. Menq, "Large travel ultra precision $x-y-\theta$ motion control of a magnetic-suspension stage," *IEEE/ASME Trans. Mechatronics*, vol. 8, no. 3, pp. 334–341, Sep. 2003.
[14] X. X. Shan, S. K. Kuo, J. Zhang, and C. H. Menq, "Ultra precision motion control of a multiple degrees of freedom magnetic suspension stage," *IEEE/ASME Trans. Mechatronics*, vol. 7, no. 1, pp. 67–78, Mar. 2002.
[15] M. B. Khamesee, N. Kato, Y. Nomura, and T. Nakamura, "Design and control of a microrobotic system using magnetic levitation," *IEEE/ASME Trans. Mechatronics*, vol. 7, no. 1, pp. 1–13, Mar. 2002.
[16] R. L. Hollis, S. E. Salcudean, and A. P. Allan, "A six degree-of-freedom magnetically levitated variable compliance fine-motion wrist: Design, modeling, and control," *IEEE Trans. Robot. Autom.*, vol. 7, no. 3, pp. 320–332, Jun. 1991.
[17] R. L. Hollis, "Magnetically levitated fine motion wrist with programmable compliance," U.S. Patent 4 874 998, Oct. 17, 1989.
[18] D. N. Galburt, "Microlithographic apparatus," U.S. Patent 4 952 858, Aug. 28, 1990.
[19] D. N. Galburt and G. O'Connor, "Wafer stage with reference surface," U.S. Patent 5 285 142, Feb. 8, 1994.
[20] H. Kano, "Optical pickup apparatus of thin type with magnetic circuit," U.S. Patent 6 285 644 B1, Sep. 4, 2001.
[21] S. Verma, W.-J. Kim, and H. Shakir, "Multi-axis maglev nanopositioner for precision manufacturing and manipulation applications," *IEEE Trans. Ind. Appl.*, vol. 41, no. 5, pp. 1159–1167, Sep. 2005.
[22] J. Gu, W.-J. Kim, and S. Verma, "Nanoscale motion control with a compact minimum-actuator magnetic levitator," *ASME J. Dyn. Syst., Meas., Control*, vol. 127, no. 3, pp. 433–442, Sep. 2005.
[23] H. A. Haus and J. R. Melcher, *Electromagnetic Fields and Energy*. Englewood Cliffs, NJ: Prentice-Hall, 1989.
[24] C. Y. Kim and K. H. Kim, "Gain scheduled control of magnetic suspension systems," in *Proc. Amer. Control Conf.*, Jun. 1994, pp. 3127–3131.
[25] H. K. Khalil, *Nonlinear Systems*. Englewood Cliffs, NJ: Prentice-Hall, 2002.
[26] M. French and E. Rogers, "Approximate parameterizations for adaptive feedback linearization," in *Proc. 36th Conf. Decision & Control*, San Diego, CA, Dec. 1997, pp. 4665–4670.
[27] A. J. Krener. A Brief Tutorial on Linear and Nonlinear Control Theory. [Online]. Available: http://www.samsi.info/200 304/multi/akrener.pdf
[28] S. A. Bortoff, "Approximate state-feedback linearization using spline functions," *Automatica*, vol. 33, no. 8, pp. 1449–1458, Aug. 1997.

Manuscript received November 21, 2005; revised April 19, 2006. Corresponding author: W.-J. Kim (e-mail: wjkim@tamu.edu).

Shobhit Verma (S'02) received the B.Tech. degree in mechanical engineering and the M.Tech. degree in computer integrated manufacturing from the Indian Institute of Technology, Bombay, India, in 2002 and the Ph.D. degree in mechanical engineering from Texas A&M University, College Station, in 2005.

He worked in Crompton Greaves, India, as a summer trainee during summer 2000. He is currently with KLA-Tencor, San Jose, CA. His research interests are magnetic levitation, precision positioning, and nanofabrication.

Dr. Verma is a student member of ASME. During his undergraduate study, he was the leading member of the winner team of the region XIII (outside North America) in the ASME student design contest and finalist in 2000. In 2001, his team represented the region XIII again and was ranked fifth in the international finals during the ASME conference at New York.

Huzefa Shakir (S'02) received the B.Tech. (Honors) degree in mechanical engineering from the Indian Institute of Technology, Kharagpur, India, in 2000. He is currently working toward the Ph.D. degree at Texas A&M University, College Station.

In September 2002, he joined Precision Mechatronics and Nanotechnology Lab., Department of Mechanical Engineering, Texas A&M University, College Station, where he is currently working as Graduate Assistant. He worked as a teaching assistant for one year for the Dynamic Systems and Controls and Engineering Dynamics courses. He was an Assistant Manager at Maruti Udyog Limited, (Suzuki Motor Corporation) India, a leading automobile manufacturing company, for two years following receipt of the Bachelor's degree. His research interests include analysis and design of control systems, and nanoscale manufacturing and motion control.

Mr. Shakir is a student member of ASME, a member of the Honor Society of Phi Kappa Phi, and Fellow, Center for Teaching Excellence, Texas A&M University. He is the recipient of a Best Presentation Award in the American Control Conference 2005.

Won-Jong Kim (S'89–M'97–SM'03) received the B.S. (*summa cum laude*) and M.S. degrees in control and instrumentation engineering from Seoul National University, Seoul, Korea, in 1989 and 1991, respectively, and the Ph.D. degree in electrical engineering and computer science from the Massachusetts Institute of Technology (MIT), Cambridge, in 1997.

In September 2000, he joined the Department of Mechanical Engineering, Texas A&M University (TAMU), College Station, where he is currently Associate Professor. Following receipt of the Ph.D. degree, he was with SatCon Technology Corporation, Cambridge, MA, for three years. His teaching and research interests focus on analysis, design, and real-time control of mechatronic systems, networked control systems, and nanoscale engineering and technology. He holds three U.S. patents on precision positioning systems.

Dr. Kim received the Grand Prize from the Korean Institute of Electrical Engineers' Student Paper Contest in 1988. His 1997 MIT dissertation earned him the Gold Prize from Samsung Electronics' Humantech Thesis Prize. He was a semifinalist of the NIST's Advanced Technology Program 2000 Competition. NASA granted him the Space Act Award in 2002. He was appointed a Select Young Faculty Fellow by TAMU College of Engineering and the Texas Engineering Experiment Station twice in 2003 and 2005. He received the Professional Engineering Publishing Award for the best paper published in the 2004 volume of *Journal of Engineering Manufacture* in 2005. He is Chair of the ASME Nanoscale Control Technical Panel and Member of the IEEE Nanotechnology Council. He is a member of Pi Tau Sigma and ASME.